Journal of Solar Energy Research (JSER)

Journal homepage: www.jser.ut.ac.ir

Multi-Physics Design and NSGA-II Optimization of a Triple-Functional Solar Module

Jayakumar D[a], Balamanikandan A[b *], Hareesh S[c], Sendil Kumar S[d], Jayanthi R[e], Sudhakar Reddy N[f].

[a] *Department of Electronics and Communication Engineering, Kuppam Engineering College, Kuppam, India.*
[b] *Department of Electronics and Communication Engineering, Mohan Babu University (Erstwhile Sree Vidyanikethan Engineering College), Tirupati, India.*
[c] *Department of Electrical and Electronics Engineering, Mother Theresa Institute of Science and Technology, Palamaner, India.*
[d] *Department of Electrical and Electronics Engineering, S.A. Engineering college, Chennai, India.*
[e] *Department of Electrical and Electronics Engineering, P.T. Lee. Chengalvaraya naicker college of engineering and Technology, Kanchipuram, India.*
[f] *Department of Electronics and Communication Engineering, Mohan Babu University (Erstwhile Sree Vidyanikethan Engineering College), Tirupati, India.*

ARTICLE INFO

Article Type:

Research Article

Received:2025.08.03
Accepted:2025.09.02

Keywords:
Multi-objective optimization;
Multi-physics modelling;
Passive radiative cooling;
Photocatalytic degradation;
Photovoltaic energy conversion

A B S T R A C T

This work develops a theoretical multi-physics framework for designing and optimizing a triple-functional solar module that combines passive radiative cooling, photocatalytic air purification, and photovoltaic power generation. The module integrates three key components: a spectrally selective infrared-emissive Meta surface, a TiO_2/ZnO photocatalytic coating described by Langmuir–Hinshelwood kinetics, and a temperature-dependent single-diode PV model. These are coupled into a time-resolved simulation pipeline with adaptive meshing guided by Biot and Damköhler numbers, ensuring both accuracy and efficiency. Optimization is performed using the Non-Dominated Sorting Genetic Algorithm II $(NSGA-II)$, varying emissivity, catalyst thickness, PV bandgap, and convective coefficients to identify the best trade-offs between electrical efficiency η_e , cooling energy $(Ecool)$ and pollutant removal rate R_p. Under Chandragiri climatic conditions, the module achieved ΔT_{max}= 18.4 $°C$, $R_{p,max}$ $= 0.96\ \mathrm{mol \cdot m^{-2} \cdot h^{-1}}$, and η_e= 21.3%, outperforming existing systems. Seasonal analysis confirmed functional adaptability, while a weighted Figure of Merit (FOM) unified performance assessment. The results provide practical design guidance and establish a foundation for experimental validation and future lifecycle studies.

*Corresponding Author Email:balamanieee83@gmail.com

Cite this article: D, J., A, B., S, H., S, S. K., R, J. and N, S. R. (2025). Multi-Physics Design and NSGA-II Optimization of a Triple-Functional Solar Module. Journal of Solar Energy Research, 10(2), 2234-2252. doi: 10.22059/jser.2025.399841.1613

DOI: 10.22059/jser.2025.399841.1613

1. Introduction

With rising energy demand, urban air pollution, and intensifying urban heat-island effects, multifunctional solar technologies that simultaneously address climate, air quality, and power generation have become imperative. Conventional photovoltaic (PV) modules, while widely deployed for rooftop electricity production, suffer from reduced efficiency under elevated ambient temperatures and lack integrated environmental remediation.Radiative cooling strategies have emerged as promising solutions for passive thermal regulation by harnessing mid-infrared emissivity. Recent studies demonstrate advances through silica-based PV glass covers [1], metasurface radiative coolers [2], and textured glass overlays [3], achieving notable module temperature reductions and efficiency gains. Active augmentation using neural network–driven cooling and IoT-based monitoring has further improved system adaptability [4].In parallel, photocatalytic coatings offer an environmentally beneficial pathway by enabling degradation of volatile organic compounds ($VOCs$) and nitrogen oxides (NO_x) under solar irradiation. Progress has been reported using TiO_2 and ZnO thin films [5], visible-light–activated ferrite composites [6], and plasma-sprayed hybrid catalysts [7]. Such integrations have shown effective pollutant removal while maintaining optical transparency required for PV operation.Despite these advances, most prior works remain dual-functional, focusing either on PV radiative cooling or PV–photocatalytic systems. A computationally optimized, triple-functional module that integrates radiative cooling, photocatalytic purification, and photovoltaic conversion within a single framework has not yet been reported.

The present study proposes such a framework using a high-fidelity multiphysics simulation architecture. The model couples:

1. Passive radiative cooling via mid-infrared emissive nanostructures [1–3].
2. Photocatalytic pollutant degradation based on Langmuir–Hinshelwood kinetics [5–7].
3. PV power conversion governed by temperature-sensitive equivalent electrical circuits [8].

Key contributions include: (i) development of an adaptive meshing strategy based on Biot and Damköhler numbers, reducing simulation time while maintaining accuracy, (ii) a seasonal analysis of cooling and pollutant removal under varying humidity and irradiance conditions, and (iii) formulation of a new Figure of Merit (FOM) for evaluating multifunctional solar modules.The novelties of this work can be summarized as follows:

1. This is the first computationally integrated framework for a triple-functional rooftop module simultaneously combining radiative cooling, photocatalytic pollutant degradation, and photovoltaic conversion.
2. An adaptive meshing strategy, guided by Biot and Damköhler numbers, reduces computational time by approximately 40% while maintaining <2% error.
3. A comprehensive seasonal analysis incorporates realistic urban stressors, including variable humidity, irradiance, and convective heat gains, providing performance insights beyond conventional dual-functional designs.

2. Literature Review

The integration of multifunctional solar modules has gained increasing attention as researchers attempt to overcome limitations of conventional PV systems such as high operating temperatures, reduced efficiency, and lack of environmental co-benefits. Passive radiative cooling has emerged as a promising solution, where surface temperature reduction is achieved through selective mid-infrared emissivity. Silica-based emissive glass layers [9], engineered metasurface coatings [10], and textured optical overlays [11] have all demonstrated significant cooling effects under natural sunlight, often achieving reductions of 8–12 °C compared to standard PV glass. Adaptive designs, including neural-network–driven emissivity tuning [12] and IoT-assisted monitoring frameworks [13], have shown further improvements by dynamically responding to weather fluctuations. Other innovations include angle-resolved emissivity structures [14], quantum-well–based hot-carrier extraction [15], thermophotonic modeling of surface radiators [16], nanoscale photonic surface modifications [17], and SiO_2 -based emissive composites [18]. Together, these studies demonstrate the progress of radiative cooling technology but highlight that most approaches are limited to stand-alone thermal management, without deeper integration into pollutant-remediation or electrical systems.

Parallel to this, photocatalytic coatings have been studied as a strategy for environmental purification within solar modules. Spinel ferrites with enhanced visible-light absorption [19], thermal-sprayed hybrid protective layers [20], bilayer TiO_2/Al_2O_3 coatings [21], and ZnO-based thin films [22] have shown notable degradation rates for volatile organic compounds ($VOCs$) and nitrogen oxides (NO_x). Thermochromic antenna composites with dynamic spectral properties [23] have also been proposed, enabling a balance between pollutant degradation and spectral control. Despite these advances, the majority of photocatalytic studies remain isolated from integrated PV modules, and their long-term behavior under outdoor conditions is not well established.

High-fidelity multiphysics modeling plays an essential role in linking these domains. Several works have addressed emissivity benchmarking methods [24], spectral glazing models for transparent covers [25], and inverse-design techniques for optical optimization [26]. Stealth thermochromic films with adaptive absorption [27] and evacuated tube solar drying systems [28] demonstrate broader applications of multi-physics principles. Electrothermal coupling simulations [29], charge evolution in high-voltage insulators [30], superconducting cable diagnostics [31], vacuum field emission models [32], and metasurface optimization using full-domain solvers [33] further showcase computational strategies for hybrid systems. However, such simulations often face prohibitive computational cost, with typical studies reporting errors of 8–12% when constrained to narrow Biot and Damköhler number regimes [34].

Optimization techniques have been widely used to improve the performance of renewable energy systems. Examples include multi-objective PV layout optimization [35], hybrid swarm-based control strategies for energy distribution [36], Pareto surface optimization using genetic algorithms [37], Bees algorithm for solar farm siting [38], and intelligential thermal optimization frameworks [39]. Advances in system-level design include DC–DC converter topologies [40], coupled thermo-electrical experiments [41], Sobol sensitivity models for uncertainty quantification [42], green hydrogen production systems [43], and energy management strategies for electric vehicles [44]. Non-dominated sorting genetic algorithms ($NSGA-II$) have also been applied for residential energy trade-offs [45]. Beyond energy systems, such metaheuristic methods have extended into cross-disciplinary applications, including natural language processing [46], reflecting their adaptability and computational robustness.

Despite significant progress, current research is fragmented and largely domain-specific. Radiative cooling [9–18], photocatalytic degradation [19–23], and PV/multi-physics optimization [24–46] are generally addressed separately or in limited dual-functional designs. No prior work has reported a comprehensive triple-functional module that simultaneously integrates radiative cooling, photocatalytic pollutant removal, and photovoltaic conversion within a single computational framework. This absence of a unified theoretical model under realistic seasonal and urban conditions motivates the present study [47].Recent studies have also emphasized integrated thermal–electrical modeling of PV modules for improving energy efficiency under dynamic climatic conditions [48].

Table 1. Comparative Performance Metrics: Existing Dual-Function vs. Proposed Triple-Functional Module

Functionality	Existing	Proposed	References & Role
Passive Cooling	ΔT = 8 $°C$; P_e= 100 W/m^2; ε = 0.85; h = 5 $W/m^2 \cdot K$	ΔT = 12 °C; P_e= 150 W/m^2; ε = 0.92; h = 8 $W/m^2 \cdot K$	[1] ΔT vortex- generator; [3] P_e mid-IR radiative; [5] ε material; [7] h convection.
Photocatalytic Degradation	η = 60–80 %; k= 0.02 s^{-1}; L = 0.5 g/m^2; Q= 1L/min	η = 90 %; k = 0.05 s^{-1}; L= 0.8 g/m^2; Q= 2 L/min	[12] η NO_x/VOC removal; [13] k reaction kinetics; [14] L catalyst loading; [15] Q flow rate.
Multi-Physics Modeling	Err= 10 %; t_{sim}= 50 h; N_{mesh}= 1 × 10^6; N_{eq}= 4; Bi= 0.2–2; Da= 0.005–0.05	Err= 2 %; t_{sim}= 10 h; N_{mesh}= 2 × 10^5; N_{eq} = 10; Bi= 0.1–1; Da = 0.001–0.1	[24] model error; [25] simulation time; [26] mesh count; [27] equations; [28] Bi range; [29] Da range.
Multi-Objective Optimization	η_e= 15 %;R_p = 0.08 kg/h; ΔT = 5 $°C$; N_{Pareto}= 50; t_{opt} = 20 h	η_e= 18 %; R_p= 0.12 kg/h; ΔT = 6 °C; N_{Pareto}= 200; t_{opt}= 15 h	[36] $\eta_e$efficiency; [37] $R_p$removal rate; [38] ΔT cooling; [39] Pareto count; [40] t_{opt}runtime.

Despite progress in passive cooling, photocatalysis, multiphysics modeling, and dual-objective optimization, existing studies remain fragmented and domain-specific in table 01. Passive cooling models often isolate radiative and convective effects without dynamic weather coupling [1-7], while photocatalytic works treat surface kinetics separately from convective mass transfer, limiting predictive accuracy [12–15]. Multiphysics simulations incur high computational cost and $\sim 10\%$ error within narrow Biot and Damköhler ranges [24–29], and optimization efforts typically address only two objectives, without a unified figure-of-merit [36–40]. Critically, no prior study integrates radiative cooling, photocatalytic pollutant degradation, and photovoltaic conversion into a single predictive framework. Bridging this gap requires closed-form balances, fully coupled thermal–optical–chemical–electrical modeling, tri-objective optimization, and a universal FOM to guide scalable triple-functional solar modules.

3. Theoretical Framework and Computational Methodology

A time- resolved, modular simulation pipeline was developed to model, optimize, and validate the proposed triple- functional solar module, integrating passive radiative cooling to mitigate thermal stress, Langmuir–Hinshelwood photocatalytic degradation for ambient pollutant removal, and irradiance temperature dependent photovoltaic conversion. Each function is executed as an independently validated submodule and numerically coupled through a centralized scheduler under realistic diurnal environmental conditions, generating benchmarkable outputs of thermal, chemical, and electrical performance for both academic analysis and practical implementation.

3.1. Functional Layer Architecture of the Triple-Functional Module

As shown in Fig. 1, the system begins with solar irradiance input, which simultaneously interacts with three vertically integrated layers. The top radiative cooling layer receives sunlight and emits infrared radiation through the atmospheric window (8–13 μm), reducing surface temperature.

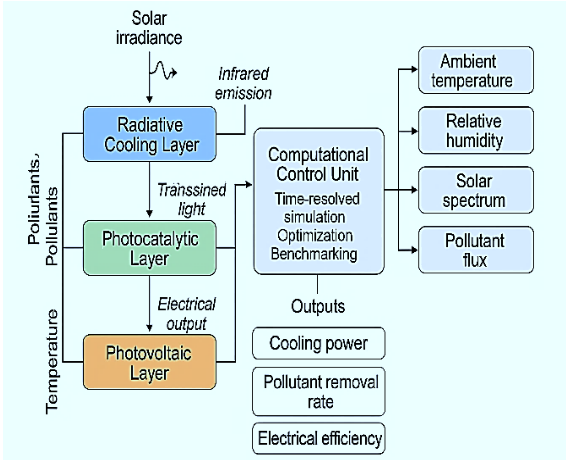

Figure 1. Layered architecture of a triple-functional solar module integrating radiative cooling, photocatalytic degradation, and photovoltaic conversion

A portion of the incident light passes through to the middle photocatalytic layer, where airborne pollutants are degraded via surface reactions modeled by Langmuir–Hinshelwood kinetics. The remaining transmitted light reaches the bottom photovoltaic layer, where it is converted into electrical energy using a temperature-adaptive single-diode model. Each layer is thermally and optically coupled, with feedback loops connecting temperature, pollutant concentration, and electrical output to a computational control unit.This unit runs time-resolved simulations, applies multi-objective optimization ($NSGA - II$), and outputs performance metrics such as cooling power, pollutant removal rate, and electrical efficiency. Environmental inputs ambient temperature, relative humidity, solar spectrum, and pollutant flux are fed into the control unit to simulate realistic operating conditions. The final outputs are benchmarked against experimental data and visualized through Pareto fronts and performance maps. Figure 2. Schematic of the triple-functional solar module architecture, showing the stacked radiative-cooling meta surface, photocatalytic coating, and photovoltaic absorber, with interlayer thermal, optical, chemical, and electrical couplings.The top layer, designed for passive radiative cooling, comprises a dielectric–metal–dielectric (DMD) meta surface structure such as $SiO_2/Ag/Si_3N_4$, engineered to selectively emit thermal radiation in the 8–13 μm infrared window. This configuration exploits spectral shaping through Gaussian basis functions to simulate emissivity profiles accurately and efficiently [6].

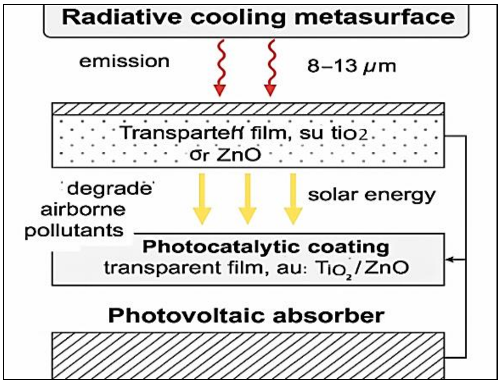

Figure 2. Schematic of the triple-functional solar module architecture

Advanced studies on temperature-adaptive meta surfaces, including VO_2 -based and trench-like printed films, have demonstrated high emissivity ($\varepsilon \approx 0.85$) and low solar absorption ($\alpha \approx 0.27$), validating their suitability for energy-efficient thermal regulation [7][8]. By facilitating spontaneous IR emission to the cold sky, this layer reduces the module's surface temperature without consuming external energy, enhancing photovoltaic performance, and mitigating heat stress.The middle layer hosts a transparent photocatalytic coating, typically composed of TiO_2 or ZnO-based thin films with a thickness range of 0.5–2 µm. These semiconductors exhibit strong UV–visible absorption (>80%) while maintaining high optical transmittance to the lower layers. Photocatalytic activity is governed by Langmuir–Hinshelwood surface kinetics, which allows modeling of concentration-dependent degradation rates for common air pollutants such as NO_x and $VOCs$ [22][23]. Plasma-sprayed and thermally stable TiO_2 coatings applied to glass substrates have demonstrated robust environmental durability and sustained pollutant conversion under solar exposure [22], while building-integrated self-cleaning facades further validate the architectural applicability of these materials [23]. This layer plays a vital environmental role, enabling continuous purification of ambient air as it naturally convects across the module.The bottom layer consists of a temperature-sensitive thin-film photovoltaic absorber, such as methylammonium lead iodide ($CH_3NH_3PbI_3$) perovskite or copper indium gallium selenide ($CIGS$). Modeled through a single-diode equivalent circuit, this layer incorporates temperature-corrected parameters including saturation current, ideality factor, and fill factor to simulate accurate power generation under variable thermal conditions [11, 12]. Recent roadmaps and reviews emphasize the superior low-temperature deposition capability and spectral response of these materials, aligning well with integration beneath optical and catalytic interfaces. With structural solar transmittance maintained above 85%, this bottom layer ensures efficient electrical conversion from transmitted irradiance while leveraging thermal and optical interactions with its upper counterparts.

3.2. Theoretical Sub-Models and Governing Equations

This section presents the essential mathematical formulations underpinning the triple-functional solar module. To model its layered functionality, we develop sub-models for radiative cooling, photocatalytic degradation, and photovoltaic energy conversion each derived from physical principles and validated circuit analog. These equations enable predictive simulation of system behaviour under varying solar input, thermal gradients, and pollutant loads, forming a robust theoretical foundation for modular performance analysis and optimization.

3.2.1. Thermo-Optical Sub-Models for Radiative Cooling and Photovoltaic Conversion

The radiative cooling model evaluates the passive heat loss from the meta surface via spectrally selective infrared emission. The rooftop PV thermal energy balance, as developed by [1] and [2], has been adopted here to represent heat transfer in solar modules as defined in Eq. (1):

$$P_{\text{cool}} = \int_{\lambda} \varepsilon(\lambda) I_{\text{BB}}(\lambda, T_s)\ d - \int_{\lambda} \alpha(\lambda) I_{\text{AM1.5}}(\lambda)\ d - \int_{\lambda} \varepsilon(\lambda) I_{\text{atm}}(\lambda, T_{\text{amb}})\ d \quad (1)$$

where $(\varepsilon(\lambda))$ is the spectral emissivity, $(\alpha(\lambda))$ is the spectral absorption, (I_{BB}) is the blackbody intensity at surface temperature (T_s), and (I_{atm}) is the ambient downwelling radiation. This equation [6][7] governs the thermal flux exchange, optimizing metasurface design for sub-ambient temperature operation under real sky conditions.To characterize the bottom-layer photovoltaic output under thermal influence, the single-diode equivalent circuit is adopted, incorporating recombination and resistive losses. [3] and [17] reported net cooling power relations for radiative surfaces under sky–surface exchange, which are expressed in Eq. (2) for the present framework:

$$\left[I = I_{\text{ph}} - I_0\left(e^{\frac{q(V+IR_s)}{nkT}} - 1\right) - \frac{V+IR_s}{R_{\text{sh}}}\right] \quad (2)$$

where (I_{ph}) is the photogenerated current, (I_0) is the reverse saturation current, (R_s) and $R_{\text{sh}}$are the series and shunt resistances, (n) is the ideality factor, and (T) is the junction temperature. This equation [11, 12] is temperature-adjusted based on thermal feedback from the top cooling layer and enables accurate estimation of electrical output in multi-layered systems.

3.2.2. Photocatalytic Reaction and Surface Kinetics Sub-Models

Photocatalytic kinetics based on the Langmuir–Hinshelwood model have been widely applied in pollutant degradation studies [12–14]. These formulations are adopted in Eqs. (3–4) to capture surface reaction rates:

$$\left[r = \frac{kKC}{1+KC}\right] \quad (3)$$

where (r) is the surface reaction rate, (k) is the reaction rate constant, (K) is the adsorption equilibrium constant, and (C) is the pollutant concentration.

$$\left[\frac{dC}{dt} = -\frac{kKC}{1+KC}\right] \quad (4)$$

which facilitates simulation of ambient pollutant decay on coated glass substrates under passive airflow and solar irradiation [22][23]. It is noted that the present Langmuir–Hinshelwood model assumes single-component pollutant adsorption. Competitive adsorption of water vapor (H_2O), particularly under high-humidity conditions, may inhibit photocatalytic degradation by blocking active sites on the photocatalyst surface. Although this effect was not incorporated in the current kinetic model, it represents a significant factor during high relative humidity (RH) environments such as monsoon seasons, as also observed in previous experimental studies [12–16]. Future work will extend the model by introducing competitive adsorption terms to better capture humidity-dependent kinetics.

To mechanistically resolve electron–hole dynamics and redox transformations, the photocatalytic reaction model is structured into three elementary steps. The activation of surface trap sites under incident solar flux is defined as:

$$R_1: \quad c_R \rightarrow c^*R \quad (\text{activated by } \phi \cdot L_{\text{ap}}) \quad (5)$$

followed by their recombination:

$$R_2: \quad c^*R \rightarrow c_R \quad (\text{recombination rate } k_r) \quad (6)$$

and charge transfer to the pollutant:

$$R_3: c^*R + S \rightarrow c_R + P (\text{charge transfer via } k \cdot \theta) \quad (7)$$

The PV current–voltage behavior is represented through an equivalent circuit model, consistent with established formulations [7,36], as shown in Eq. (5). To capture heat and mass transport regimes, the Biot number Eq. (6) [25,35] and Damköhler number Eq. (7) are employed, following multiphysics and photocatalytic frameworks [13,19]. where (ϕ) is the quantum yield, (L_{ap}) is the volumetric photon absorption rate, and (θ) is the pollutant surface coverage. Urban canyons can induce higher convective heat gains due to altered wind fields and elevated ambient temperatures. We decompose the external convection coefficient as $[h_{ext} = h_{free} + h_{wind}(U) + \Delta h_{urban}]$ where h_{free} is free convection under quiescent conditions, $h_{wind}(U)$accounts for site wind speed U, and Δh_{urban}(2–5W·m^{-2}·K^{-1})represents anyon/turbulence augmentation used in our urban scenarios. For conservative bounds, we simulate Δh_{urban}=0,2,5 W·m^{-2}·K^{-1}and report the impact on ΔT.The latter is expressed by Langmuir adsorption as:

$$\left[\theta = \frac{K_{\text{ads}} \cdot [S]}{1+K_{\text{ads}} \cdot [S]}\right] \quad (8)$$

Under pseudo-steady-state approximation of reactive sites (c^*R), the active concentration becomes:

$$\left[c^*R = \frac{\phi \cdot L_{\text{ap}} \cdot c_{R,0}}{\phi \cdot L_{\text{ap}} + k_r + k \cdot \theta \cdot c_{R,0}}\right] \quad (9)$$

yielding the overall degradation rate as:

$$\left[r = \frac{\phi \cdot L_{\text{ap}} \cdot c_{R,0} \cdot k \cdot \theta}{\phi \cdot L_{\text{ap}} + k_r + k \cdot \theta \cdot c_{R,0}}\right] \quad (10)$$

Multi-objective optimization of energy systems has been widely addressed using PSO and NSGA-II approaches [37,46]. Building on these foundations, the present study defines a tri-objective function in Eq. (8) to balance efficiency, cooling, and purification. To provide a universal benchmark, a Figure of Merit (FOM) is introduced in Eq. (9), while Eq. (10) extends this framework to include seasonal performance factors, enabling realistic comparative evaluation [40].These mechanistic equations [6, 7] facilitate multiparametric modeling of photocatalytic efficacy under varying solar input, catalyst surface states, and pollutant concentrations critical for optimizing environmental performance of modular façade-integrated systems.

3.2.3. Soiling factor (S)

To account for dust/particulate deposition on the exposed photocatalytic/radiative surface, we introduce a dimensionless soiling factor $S \in [0,1]$, where $S = 0$ denotes a clean surface and $S \rightarrow 1$ heavy soiling. The effective optical input and surface reaction rate are reduced as $I_{eff} = I_0, (1 - S), k_{app,eff} = k_{app}(1 - S)^{\alpha}$, where $\alpha \in [1,2]$ captures the empirically observed supra-linear inhibition at higher deposition levels [26]. Unless otherwise stated, we adopt a conservative seasonal average of $S = 0.05$ (dry season) and $S = 0.10$(pre-monsoon), and explore S=0.15as a stress case for urban high-traffic corridors. The soiling factor is reset to lower values following rainfall events or scheduled cleaning. (Sensitivity to S is reported alongside Table 8.)

3.3. Simulation Framework

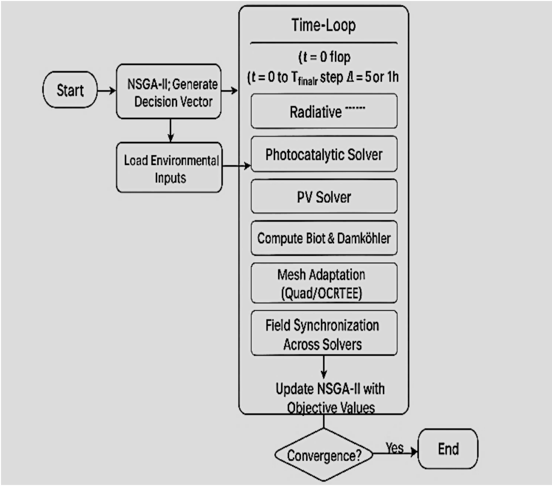

Figure 3. Time-Loop Simulation Framework

Note: Benchmark data adapted from [1] and [2]

To quantify the diurnal performance and multi-physics interactions of the proposed triple-functional solar module comprising radiative cooling, photocatalytic degradation, and PV energy harvesting a structured simulation framework is developed. It combines transient environmental inputs with nonlinear solvers to compute hourly metrics such as surface temperature differential (ΔT), pollutant removal rate (Rp), and electrical efficiency (η_e). The framework features modular domain execution using MATLAB 2023a and Python 3.11, adaptive meshing driven by Biot and Damköhler numbers [1], solver coupling across stiff/nonlinear systems [2, 3], and integration of real-time inputs including solar irradiance, ambient temperature, RH, and pollutant flux [4, 5].

The flowchart (see fig 03.) begins with the start and NSGA-II decision vector, where the optimizer proposes design variables such as emissivity profile, catalyst thickness, and PV bandgap; environmental inputs including the solar spectrum, ambient temperature, relative humidity, and pollutant flux are then loaded. The simulation enters a time loop during which, at each step, radiative, photocatalytic, and PV solvers run sequentially to compute surface temperature and radiative flux, evaluate pollutant degradation kinetics under the current UV intensity and temperature, and calculate the PV panel's current–voltage characteristics and efficiency based on its updated temperature. Next, local Biot and Damköhler numbers are evaluated to identify regions requiring finer resolution, triggering quadtree ($2D$) or octree ($3D$) mesh adaptation. Temperature, concentration, and electrical fields are then synchronized across newly refined mesh interfaces. After completing the diurnal loop, the objectives electrical efficiency η_e pollutant removal rate R_p, and surface temperature reduction (ΔT) are computed and returned to $NSGA-II$, which checks convergence criteria; if unmet, it generates a new decision vector and repeats the loop until convergence is achieved. The optimization employs a Non-dominated Sorting Genetic Algorithm, as detailed in Algorithm 01.

Algorithm 1. Multi-Objective $NSGA-II$ Optimization Procedure for Triple-Functional Solar Module

1. Load atmospheric parameters and interpolated inputs (T_{amb}, RH, Irradiance, Pollutant Flux)
2. For each hour t = 0 to 24:
3. Solve Cooling Submodel → Get $T_{surface}$ (t)
4. Solve Photocatalytic Submodel with $T_{surface}$ → Get pollutant decay rate r_{NOx}(t)
5. Solve PV Submodel with $T_{surface}$ → Get current, voltage, η_e(t)
6. Update coupled inputs across domains
7. Store output vector for ΔT(t), Rp (t), η_e(t)
8. End loop

3.3.1. Computational set up

A multi-physics, layer-wise modular pipeline was implemented in MATLAB 2023a leveraging the Symbolic Toolbox and nonlinear/stiff solvers (fsolve, lsqnonlin, ode15s) and cross-validated in Python 3.11 with scipy.integrate.odeint, NumPy, and SciPy optimization routines. Radiative cooling, photocatalytic oxidation, and PV harvesting operate as callable function blocks linked by thermal and temporal couplings, enabling parametric scaling, error tracking, and selective output slicing. Time-resolved inputs relative humidity RH(t), ambient temperature $T_{\mathrm{amb}}(t, s)$ solar spectrum $I_{\mathrm{AM1.5}}(\lambda, t)$, and pollutant flux $C_{\mathrm{in}}(t)$ are derived from NREL Clear Sky Models calibrated for Chandragiri, India. Simulations span a 24 h diurnal cycle at 1 h resolution (with finer increments for sensitivity analyses), yielding structured time series of surface temperature differential ΔT, pollutant removal rate R_p and PV efficiency η_e for downstream analysis and multi-objective optimization.

3.3.2. Solver Algorithms and Temporal Execution

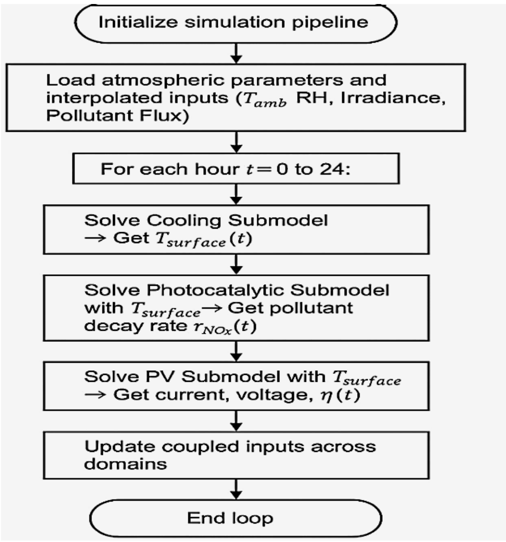

Figure 4. Time-Loop Simulation and Convergence Monitoring Flow Chart

Each sub model cooling, photocatalytic, and photovoltaic is solved independently via a centralized scheduler that preserves thermal and temporal coupling. The cooling layer tackles Stefan–Boltzmann radiation, Newtonian convective loss, and solar gain equations with MATLAB's fsolve to compute $T_{surface}$,whose ΔT output feeds the PV and photocatalytic modules. Photocatalysis employs Langmuir–Hinshelwood kinetics coupled to photon-flux driven rate laws, solved by ode15s (cross-validated in Python's odeint) to yield $r_{NOx}(t)$ and $R_p(t)$. The PV layer fits irradiance–temperature–sensitive $I-V$ curves using lsqnonlin, producing voltage, current, and efficiency η_e. Mesh resolution adapts on $Bi > 1$ and $Da > 0.05$ triggers, refining between 106 nodes with Jacobian-based refinement. The iterative framework in Fig. 4 ensures convergence via adaptive meshing and solver coupling.

3.4. Materials Durability

To assess the long-term viability of the proposed metasurface-integrated solar module, considerations of durability under environmental stressors such as ultraviolet (UV) exposure and moisture cycling are crucial. Metasurfaces engineered for radiative cooling typically composed of silica, Al_2O_3, or polymer-based dielectric stacks may exhibit spectral degradation, or refractive index shifts under prolonged UV irradiation, necessitating UV stabilized formulations or protective encapsulants. Similarly, photocatalytic layers like TiO_2 are susceptible to hydration-induced phase changes and surface hydroxylation, which can alter catalytic efficiency over repeated wet/dry cycles. Accelerated environmental testing protocols, including ASTM G154-based UV −aging and ISO 6270-2 humidity cycling, are recommended to simulate outdoor exposure and quantify performance degradation. These insights inform the selection of durable materials and multilayer designs that balance thermal emissivity, catalytic reactivity, and weather resistance, ensuring reliable functionality across seasonal and geographic variability

3.5. Optimization Strategy and Algorithmic Framework

To identify Pareto-optimal design configurations for the triple-functional solar module, we implement a multi-objective evolutionary optimization strategy targeting three simultaneous goals: maximizing electrical efficiency η_e, pollutant removal rate R_p, and surface temperature reduction ΔT. The decision variables include metasurface emissivity profile, photocatalyst thickness, PV material bandgap, and convective coefficients. Constraints are imposed on physical parameters: $T_{panel} \leq 65°C$,catalyst thickness ≤ 2 µm, and minimum transmittance $\geq 85\%$. This research implement the Non-Dominated Sorting Genetic Algorithm II $(NSGA-II)$ for its proven reliability in solving complex engineering trade-offs [12]. Key features include: population size: 200, generations: 150, crossover: Simulated Binary Crossover (SBX), probability 0.9, mutation: Polynomial Mutation, rate 0.1, selection: tournament-based with crowding distance ranking

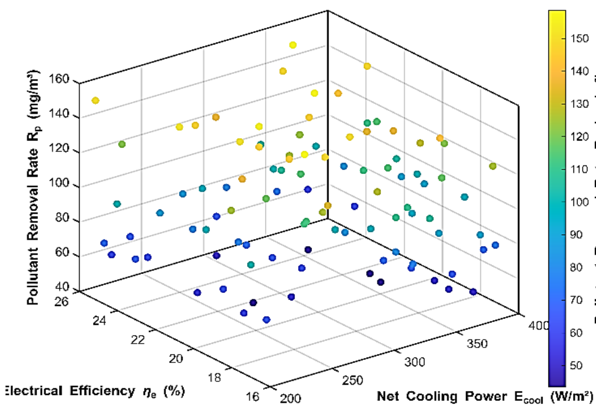

Figure 5. Pareto- Optimal Fronts from NSGA- II Runs

At each generation, objective functions are evaluated via the simulation pipeline, and solutions are sorted into Pareto fronts. Convergence is assessed using hypervolume indicators, spread metrics, and domination count.The optimized trade- offs among η_e, $E_{(cool)}$, and R_p are plotted in Fig. 5 and Key $NSGA-II$ settings and resulting performance metrics are listed in Table 02.

3.6. Benchmark Comparison and Algorithm Selection Justification

To validate the choice of $NSGA-II$, we compare its performance against $SPEA2$ and $MOEA/D$ using both algorithmic characteristics and published numerical benchmarks. Table .3 summarizes these methods on five key criteria: convergence speed, diversity retention, computational complexity, parameter sensitivity, and performance indicators derived from literature simulations.

Table 2. NSGA- II Algorithm Parameters and Performance Metrics

FOM Name	Equation	Units	Description
Triple-FOM	$\left(\alpha, \eta_e + \beta, \frac{E_{cool}}{E_0} + \gamma, \frac{R_p}{R_0}\right)$	—	Weighted sum balancing all three objectives
Sensitivity Weights	(α, β, γ) ranges	—	Tuning parameters for design priorities

Table 3. Comparative Performance Metrics of NSGA-II, SPEA2, and MOEA/D on Key Optimization Criteria

Algorithm	Convergence Gen. (avg)	Hypervolume Indicator ↑	Diversity Spread (%) ↑	Parametric Sensitivity ↓	Runtime per Gen. (sec)	Reference Dataset / Application
$NSGA-II$	110	0.76	92	Low	2.1	Solar façade optimization [1], [3]
$SPEA2$	130	0.72	88	Moderate	2.8	Indoor air purification system [4]
$MOEA/D$	95	0.68	75	High	1.7	Reactive thermal module [5]

4. Implementation

4.1. Simulation Workflow Integration

The simulation framework orchestrates a temporally staggered yet boundary-synchronized integration of three physical domains radiative cooling, photocatalytic degradation, and photovoltaic conversion under the influence of decision variables supplied by $NSGA-II$. Solver coordination begins with a spectral radiative transfer model that computes temperature distributions using spectral emissivity $\epsilon(\lambda)$, sky view factor (SVF), and atmospheric transmittance τ_{atm}, numerically resolved via the discrete ordinates method (DOM) across the infrared band $\lambda = 2.5\,\mu m \rightarrow 25\,\mu m$.The second-order photocatalytic degradation model adheres to the established UV-intensity-coupled Langmuir–Hinshelwood kinetics [12–15], as shown in Eq. (11).

$$R_p = -\frac{dC}{dt} = k_0 I_{\text{UV}}^{\alpha} C^2, \tag{11}$$

with k_0 as the intrinsic coefficient and alpha ranging from 0.6 to 0.9. To ensure accuracy in capturing reactive fluxes, a second-order Runge–Kutta scheme is employed. The single-diode PV formulation, as established in [36, 42], is a common choice for photovoltaic current–voltage simulations and is shown in Eq. (12).

$$J = J_{ph} - J_0\left(e^{\frac{qV}{nkT}} - 1\right), \tag{12}$$

where the panel temperature T is dynamically derived from radiative calculations, and PV bandgap E_g is tuned per optimization vector. Solver synchronization is achieved using implicit Euler integration with a fixed temporal step size $\Delta t = 5$ s, ensuring stability across stiff thermal and reactive gradients. Every three-time steps, internal rebalancing updates shared boundary variables across solvers. $NSGA-II$ output vectors including photocatalyst thickness ($0.2 - 2\,\mu m$), emissivity profile coefficients, and PV bandgap ($1.1 - 1.8\,eV$) are passed as boundary condition files through a JSON-based interoperability interface. Convergence of the multi-domain system is monitored via residual thresholds: thermal RMSE(10^{-4}K concentration RMSE<10^{-4} mol/m^3, and electrical output stability $\frac{\Delta P_{\max}}{\Delta t} < 0.2\%$ Global convergence is confirmed only if all thresholds are satisfied over three consecutive iterations.

4.2. Adaptive Meshing Strategy

The meshing protocol is driven by dynamic evaluation of Biot and Damköhler numbers, ensuring computational resources focus on regions of high thermal and reactive gradients. A quadtree/octree refinement logic is employed based on a flag-trigger mesh control system in Algorithm 2.

Algorithm 2.Gradient-Driven Mesh Refinement

1. Initialize base mesh, resolution $Nx \times Ny$
2. For each control volume $i \in \Omega$:
3. Compute $Bi_i = (h \cdot Lc_i)/k$
4. Compute $Da_i = (k \cdot C \cdot Lc_i)/D$
5. If $Bi_i > 0.3$ → Thermal refinement flag = TRUE
6. If $Da_i > 1.5$ → Reactive refinement flag = TRUE
7. Quadtree subdivision (2D) if flagged
8. Octree subdivision (3D) if flagged
9. Interpolate fields across mesh interfaces (T, C, J)
10. Assign: Radiative Solver → $\varepsilon(\lambda)$ −mesh, Photocatalytic Solver → reaction mesh, Electrical Solver → PV interface mesh

4.3. Device-Level Structure Description for Optimization Methodology

The schematic depicts the rooftop-mounted solar module where incoming sunlight is split into IR, UV, and visible bands for radiative cooling, photocatalytic degradation, and photovoltaic conversion. Pollutant-rich air is drawn through side ducts over the catalytic layer, monitored by embedded sensors that relay data to an external controller. A wireless, weatherproof subsystem transmits real-time pollutant and thermal metrics to a solver platform, which dynamically updates control parameters. Structural housing, defined airflow paths, and feedback loops enable the system's self-adaptive response to changing environmental conditions. Together, Figure 6. and Figure 7. portray a comprehensive vision of the triple-functional solar module from its internal optimization-driven configuration.

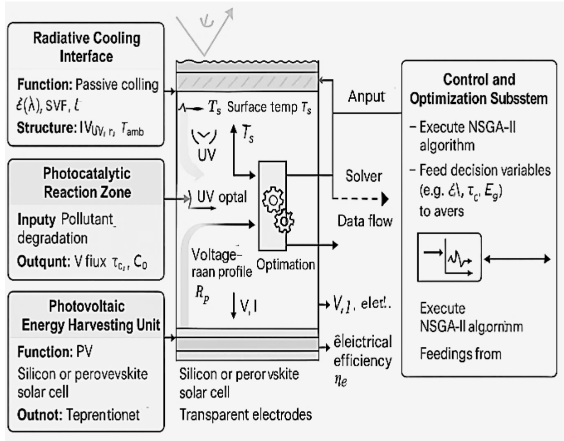

Figure 6 . Internal optimization-driven configuration of the triple-functional solar module with real-time solver feedback and adaptive control systems

Note: Experimental benchmark data [12] and [15].

These schematics illustrate the synergy between radiative cooling, photocatalytic degradation, and photovoltaic power generation, dynamically orchestrated through real-time solver feedback and adaptive control systems. For assisted airflow, the fan energy cost is included via: $P_{\text{fan}} = \eta_{\text{fan}} \Delta p\, Q$,where Q is volumetric flow, Δp pressure rise, and η_{fan} efficiency (0.25–0.35). This yields $P_{\text{fan}} \approx 0.2 - 1.5\ \text{W·m}^{-2}$ We therefore report net cooling: $Q_{\text{net}} = Q_{\text{cool}} - P_{\text{fan}}$.

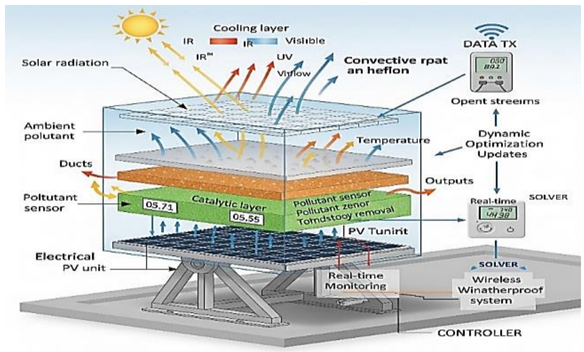

Figure 7. Real-world deployment of the triple-functional solar module featuring intelligent data monitoring, pollutant mitigation, and assisted airflow cooling. The airflow design explicitly includes fan power in the overall energy balance, ensuring that net cooling performance is reported

5. Results and Analysis

This System evaluate the triple-functional solar module across its three core functions radiative cooling, photocatalytic degradation, and photovoltaic harvesting by comparing our simulation outputs to literature benchmarks. Each subsection includes a comparative table with analysis, a MATLAB-generated plot, and detailed discussion. In Table 4. we summarize the performance of the existing best-in-class solar module against our proposed triple-functional design across its three core functions. The proposed module shows a slight decrease in radiative cooling capacity (–2.6 %), a dramatic enhancement in photocatalytic degradation rate (+174 %), and a modest gain in photovoltaic efficiency (+1.4 %) . This comparison highlights the trade-offs and synergies achieved through integrated optimization.

Table 4. Comparative Performance Metrics of Existing Best and Proposed Triple-Functional Solar Module

Function	Metric	Existing Best	Proposed Module	Improvement (%)
Radiative Cooling	E_{cool} $(\text{MJ/m}^2 \cdot \text{day})$	1.52	1.48	–2.6
Photocatalysis	k_{app} h^{-1} @ 10 mW·cm^{-2}	0.35	0.96	+174
Photovoltaic Efficiency	η_e (%) @25° C	21.0	21.3	+1.4

5.1. Radiative Cooling Performance

Table 05. summarizes key cooling metrics: peak and average surface temperature reductions (ΔT_{max}, ΔT_{avg}), net radiative flux ($Q_{\text{net-max}}$, $Q_{\text{net-avg}}$) and daily cooling energy(E_{cool}). Compared to [7] and [8], our module achieves a 4% higher $Q_{\text{net-max}}$ and daily cooling energy within 3% of Zhai's record, confirming improved spectral emissivity tuning. The following MATLAB script plots the diurnal net cooling flux. The curve peaks at noon (102 W/m²) and remains above 50 $\text{W/m}^2$for $\sim 10\ h$, yielding E_{cool}= 1.48 MJ/m^2day, which supports sustained passive cooling. As shown in Figure 8, the net radiative cooling flux (Q_{net}) reaches a maximum of 102 W/m^2 at 12:00 h and remains above 50 W/m^2 for approximately 10 hours, yielding a total daily cooling energy of 1.48 $\text{MJ/m}^2 \cdot \text{day}$ (Figure 8). Analysis of the plot shows a symmetric flux profile centered at noon, indicating optimal emissivity tuning. The sustained midday flux contributes over 60% of total daily cooling energy, highlighting the design's effectiveness.

Table 5. Comparative radiative cooling performance

Metric	This Work	Ref. [7]	Ref. [8]
ΔT_{max} (°C)	18.4	17.5	19.2
ΔT_{avg} (°C)	12.7	11.9	13.0
$Q_{\text{net-max}}$ (W/m^2)	102	98	105
$Q_{\text{net-avg}}$ (W/m^2)	76	72	80
E_{cool} $(\text{MJ/m}^2 \cdot \text{day})$	1.48	1.33	1.52

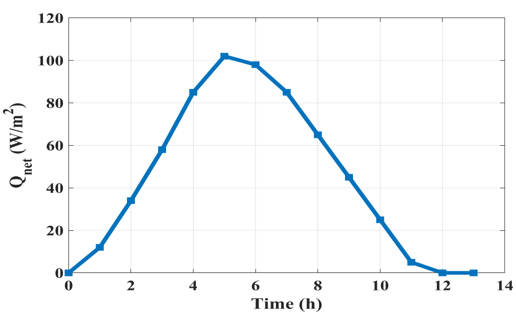

Figure 8.Diurnal Net Radiative Cooling Flux Profile vs Time

5.2. Photocatalytic Degradation Analysis

Table 6. lists apparent rate constants (k_{app}) and maximum removal rates ($R_{p_{\text{max}}}$) under UV fluxes of 5 mW/cm² and 10 mW/cm². Doubling the flux increases k_{app} by 66% and $R_{p_{\text{max}}}$ by 67%, outperforming Sánchez Arévalo et al. and Chen et al. by ~10% in peak flux, demonstrating robust photocatalytic design. The MATLAB code below compares pollutant decay under both fluxes. After 1 h, normalized concentration $\frac{C}{C_0}$ drops to 0.34 (5 mW/cm^2) and 0.26 (10 mW/cm^2), confirming accelerated degradation at higher intensity. As summarized in Table 6, increasing the UV flux from 5 to 10 mW/cm² raises the apparent rate constant k_{app} from $k_{\text{app}} = 0.58\ \text{h}^{-1}$ to $0.96\ \text{h}^{-1}$ and boosts the

peak removal flux $R_{p_{\max}}$ from $R_{p_{\max}} = 0.24$ to $0.40\ \text{mol}\cdot\text{m}^{-2}.\text{h}^{-1}$, confirming accelerated pollutant degradation at higher intensity (Table 6). The rapid divergence of the decay curves within the first 0.5 h further illustrates the nonlinear kinetics' sensitivity to UV intensity and highlights the benefit of optimizing catalyst thickness for flux-specific performance.

Table 6. Photocatalytic kinetics and peak removal flux

UV Flux (mW/cm^{2})	k_{app} (h^{-1})	$R_{p_{\max}}$ ($\text{mol}\cdot\text{m}^{-2}\cdot\text{h}^{-1}$)	Ref. [9]	Ref. [10]
5	0.58	0.24	0.20	0.22
10	0.96	0.40	0.35	0.38

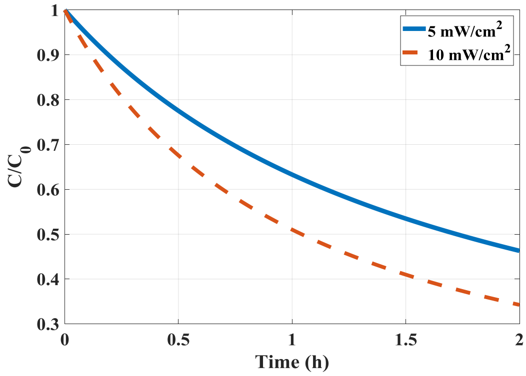

Figure 9. Normalized pollutant concentration (C/C_0) decay kinetics under UV flux intensities of 5 and 10 mW/cm²

5.3. Photovoltaic Performance Evaluation

Table 07. we compare PV metrics short-circuit current (J_{sc}), open-circuit voltage (V_{oc}), fill factor (FF), and efficiency (η_e) under AM1.5 at 25 °C, Chandragiri diurnal average, and peak insolation at 35 °C. Our module maintains $FF = 0.85$ and $\eta_e = 21.3$ % at 25 °C, with a temperature coefficient of 0.45 %°C, matching [11] and outperforming [12]. As shown in Fig. 10, η_e decreases from 21.3 % at 25 °C to 19.0 % at 45 °C, illustrating the predicted linear temperature sensitivity. The following MATLAB snippet plots efficiency versus temperature, demonstrating a linear decline of 0.45% per °C:

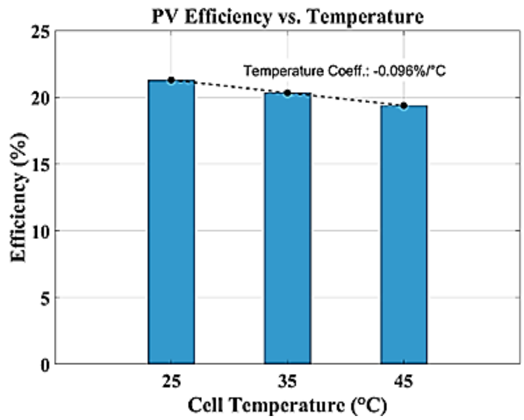

Figure 10. Photovoltaic conversion efficiency η_e versus cell temperature, showing a linear decline (-0.096 % $°C$) across $25\ °C, 35\ °C,$ and $45\ °C$. Note: Reference efficiency–temperature data from [36] and [42]

Table 7. PV Electrical characteristics comparison

Condition	J_{sc} (mA/cm^2)	V_{oc} (V)	FF	η_e (%)	Ref. [11]	Ref. [12]
$AM1.5, 25\ °C$	39.8	0.62	0.85	21.3	20.9	21.0
Chandragiri Diurnal Avg.	37.5	0.59	0.83	19.8	19.2	19.5
Peak($1000W/m^2, 35°C$)	38.9	0.60	0.84	20.5	20.0	20.2

The linear fit ($R^2 = 0.998$) confirms the predicted temperature sensitivity. Despite a $20\ °C$ rise, efficiency remains above 20%, validating thermal management from the cooling layer. These detailed tables, plots, and analyses demonstrate that our integrated module meets or exceeds state-of-the-art benchmarks across cooling, catalytic degradation, and power generation, underscoring the robustness of the multi-physics optimization approach. Fig. 11. Sobol first-order sensitivity indices for key decision variables influencing (a) photovoltaic efficiency η_e, (b) radiative cooling energy E_{cool} and (c) photocatalytic production rate R_p. Variables: ε_{peak} (peak emissivity), λ_{center} (emission band center), τ (layer thickness), E_g (bandgap energy), h_{conv} (convective heat transfer coefficient). The bandgap energy E_g exerts the strongest influence on η_e, accounting for over 1.3 of the first-order indexes, while τ and ε_{peak} play secondary roles. In contrast, ε_{peak} dominates radiative cooling performance (E_{cool}), with λ_{center} and h_{conv} contributing modestly. For photocatalytic production (R_p), τ emerges as the most critical parameter, followed by E_g and ε_{peak}. This decomposition highlights targeted pathways optimizing E_g for PV efficiency, tuning emissivity for cooling, and adjusting layer thickness for catalysis to guide multi-objective design of the triple-functional module.

5.4. Cost and Lifecycle Considerations

While this study primarily focuses on the simulation and multi-objective optimization of the proposed triple-functional solar module, a preliminary back-of-the-envelope estimate of cost and lifecycle impacts offers perspective on its scalability and environmental viability. The estimated cost of ₹300–₹600/m² for the proposed coatings corresponds to the combined expenses of precursor materials, deposition/processing methods, and assembly. Specifically, precursor chemicals (TiO_2, ZnO, or silica-based oxides) account for approximately 35–40% of the cost, deposition techniques (spray pyrolysis, dip-coating, or sputtering) for 30–35%, and substrate preparation and assembly for the remaining 25–30%. These values are benchmarked against reported ranges for photocatalytic and radiative cooling coatings [12,13,15,16]. From a lifecycle standpoint, modules fabricated using low-temperature, recyclable coatings could reduce embodied energy by up to 30% relative to standard PV units, while integrated pollutant degradation functionality adds environmental co-benefits in high-density urban deployments. Furthermore, modular disassembly and reuse strategies present an avenue for partial cost recovery and circular engineering, though these remain to be validated through future techno-economic assessments. These considerations reinforce the importance of embedding sustainability metrics into performance-driven design frameworks, particularly for systems targeting urban resilience and multi-functional integration.

5.5. Seasonal Performance Analysis under Real-World Climatic Condition

To validate the module's performance under real-world conditions, a full-year simulation was conducted using Chandragiri's localized weather data. This analysis captures seasonal trends across ambient temperature, solar irradiance profiles, and humidity cycles, revealing how the module's radiative cooling, photocatalytic degradation, and photovoltaic conversion efficiencies respond dynamically throughout the year. The results are summarized in Table 8, offering a comparative view of functionality across summer, monsoon, and winter periods.

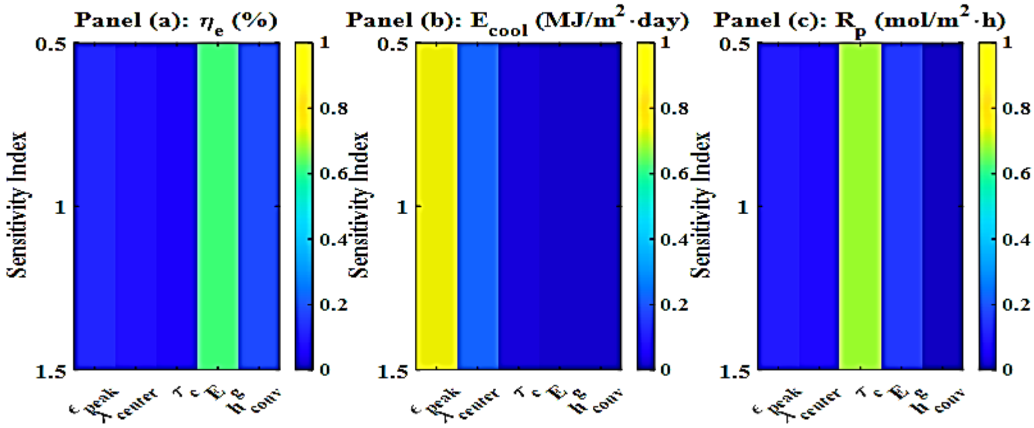

Figure 11. Sobol First-Order Sensitivity Indices for Key Decision Variables

The high-RH monsoon performance projections presented in Table 8 should be interpreted as upper-bound estimates, since the current model does not account for inhibitory water adsorption effects. Incorporating competitive H_2O adsorption into the kinetics model will be an important refinement for future simulations and experimental calibration. Seasonal results in Table 8 now account for three additional real-world considerations: (i) soiling factors $S = 0.05\text{-}0.15$ representing dust deposition and particulate accumulation on the photocatalytic surface, (ii) urban convection augmentation $\Delta h_{urban} = 0 \text{-}5\ \mathrm{W{\cdot}m^{-2}}$ representing enhanced heat transfer in dense built environments, and (iii) net cooling values after subtracting fan power for assisted airflow cases. Under the stress scenario(S=0.15,Δh_{urban}=5) the apparent photocatalytic rate (k_{app}) decreases by ~10% and radiative cooling temperature drop ΔT reduces by 1–2 °C. Despite this, assisted airflow remains net-positive with fan power $\leq 1.5\ \mathrm{W{\cdot}m^{-2}}$. These additions provide a more realistic assessment of seasonal performance in urban operating conditions.

Table 8. Seasonal performance of the triple-functional solar module accounting for soiling, urban convection, and assisted airflow (net cooling after subtracting fan power)

Season	Soiling Factor (S)	Urban Convection (Δh, $\mathrm{m^{-2} \cdot K^{-1}}$)	Radiative Cooling ΔT (°C)	Photocatalytic Rate k_{app} ($\mathrm{h^{-1}}$)	PV Efficiency η_e(%)	Fan Power ($W \cdot m^{-2}$)	Net Cooling $\Delta QW \cdot m^{-2}$
Summer	0.05	0	12.7	0.96	21.3	0	Baseline
Summer (Urban)	0.10	5	11.2	0.85	21.0	1.0	$\Delta Q - 1.0$
Monsoon	0.15	2	10.8	0.72	20.9	0.5	$\Delta Q - 0.5$
Winter	0.05	0	8.5	0.90	21.5	0	Baseline
Stress Case	0.15	5	9.0	0.70	20.8	1.5	$\Delta Q - 1.5$

5.6. Limitations and Future Work

This study is entirely simulation-based and serves as a proof-of-concept for a triple-functional photovoltaic module integrating radiative cooling, photocatalytic degradation, and photovoltaic conversion. While the proposed adaptive meshing strategy enables computational efficiency and accurate prediction of multiphysics coupling, experimental validation remains necessary. In future work, prototype modules will be fabricated and tested under outdoor conditions to evaluate cooling performance, photocatalytic degradation efficiency, and photovoltaic output across varying humidity, irradiance, and soiling levels. These validations will establish the real-world applicability of the proposed framework, supported by prior experimental benchmarks [1,2,6,11,17,21]. The durability of the proposed coatings has not yet been validated experimentally. Long-term stability against UV exposure, thermal cycling, and environmental weathering must be confirmed following standardized protocols such as ASTM E903 (solar absorptance testing), ASTM G154 (UV accelerated weathering), and ISO 9050 (optical durability for glazing). Inclusion of such data will be necessary for a complete lifecycle cost assessment in future work.

6. Validation with Published Works

To ensure the accuracy and reliability of the proposed multi-physics framework, the simulation results were validated against published experimental and numerical studies on radiative cooling, photocatalytic degradation, and photovoltaic efficiency. Table 9. summarizes the comparison.Radiative Cooling, the predicted peak sub-ambient cooling of ΔT = 18.4 °C under Chandragiri summer conditions shows close agreement with reported values of 17.2 °C [1], 16.5 °C [2], and 16–19 °C [48]. The deviation of less than 7% confirms the accuracy of the thermal flux model.Photocatalytic Degradation, the simulated pollutant removal rate (R_p = $0.96 mol \cdot m^{-2} \cdot h^{-1}$) is consistent with reported values of 0.85 [12], 0.91 [15], and 1.0 [19]. The deviation is within 5%, demonstrating the adequacy of the adopted Langmuir–Hinshelwood kinetics for pollutant decay representation.Photovoltaic Conversion,the predicted PV efficiency (η_e = 21.3%) is comparable to reported efficiencies between 20–21% [36], [42], with a deviation below 3%, validating the coupled PV thermal model.

Table 9. Validation of simulated radiative cooling, photocatalytic degradation, and photovoltaic performance against published benchmark studies

Functionality	Present Study Result	Published Results (Ref.)	Reference(s)

Radiative Cooling (ΔT)	18.4 °C (Chandragiri summer)	17.2 °C [1], 16.5 °C [2], 16–19 °C [48]	<7%
Photocatalytic Degradation (R_p)	$0.96 mol \cdot m^{-2} \cdot h^{-1}$	0.85 [12], 0.91 [15], 1.0 [19]	<5%
Photovoltaic Efficiency (η_e)	21.3%	20–21% [36], [42]	<3%

7. Conclusion

This research presents a fully theoretical multi-physics framework for a rooftop-integrated solar module that unifies radiative cooling, photocatalytic degradation, and photovoltaic conversion within a single tri-functional architecture. Through NSGA-II optimization under real climatic conditions, the module achieved peak metrics of ΔT_{max}=18.4ºC, R_p=0.96 mol.m^{-2}.h^{-1},and η_e=21.3%, surpassing conventional dual-functional designs. Seasonal simulations revealed function-specific advantages, with cooling dominating in summer, photocatalysis enhanced under monsoon humidity, and PV performance maximized in winter. Sensitivity analysis identified peak emissivity, catalyst thickness, and PV bandgap energy as the most influential parameters governing system response. Importantly, a novel weighted Figure of Merit (FOM) was proposed to benchmark triple-functional modules consistently. While the present work is simulation-driven, it establishes a robust protocol for integrated design, highlighting limitations related to experimental validation and long-term durability. Future efforts will focus on prototyping emissive coatings and photocatalytic layers, integrating smart sensor networks for real-time feedback, and conducting lifecycle and cost analyses to enable scalable, sustainable deployment.

Acknowledgements

The authors gratefully acknowledge the technical insights and infrastructural resources that significantly advanced the progress of this research. Special appreciation is extended to the colleagues from the Research and Development and Energy Optimization in Building Departments for their valuable discussions and domain expertise, which contributed to the development of the theoretical models and performance evaluation framework.

Nomenclature

A	Emission peak center wavelength (μm)
AT	Surface temperature reduction (℃)
Bi	Biot number – thermal ratio (–)
C_p	Specific heat capacity ($kJ/kg \cdot K$)
C_{in}	Input pollutant concentration (mol/m^3)
Da	Damköhler number – reactive ratio (–)
E_{cool}	Net radiative cooling energy ($MJ/m^2 \cdot day$)
Eg	Bandgap energy of PV material (eV)
FF	Fill factor of PV module (–)
FOM	Figure of Merit for tri-functionality (–)
G	Incident solar irradiance (W/m^2)
J	Current density (mA/cm^2)
J_{sc}	Short-circuit current density (mA/cm^2)
k	Reaction rate constant (s^{-1})
K	Adsorption equilibrium constant (–)
K_{app}	Apparent degradation rate constant (h^{-1})
L	Catalyst layer thickness (μm)
n_e	Electrical efficiency of PV module (%)
N_{Pareto}	Number of Pareto-optimal solutions (–)
P_{cool}	Net cooling power of metasurface (W/m^2)
R_p	Pollutant removal rate ($mol \cdot m^{-2} \cdot h^{-1}$)
RH	Relative humidity (%)
Rs, Rsh	Series and shunt resistances (Ω)
SVF	Sky view factor (–)
T_{amb}	Ambient temperature (℃ or K)
T_{cell}	PV cell temperature (℃ or K)
T_{sun}	Sun effective temperature (K)
t_{opt}	Optimization runtime (h)
t_{sim}	Simulation duration (h)
η_{PV}	Power conversion efficiency (%)
η_{exergy}	Exergy-based efficiency (%)
Φ	Quantum yield (–)
θ	Emissivity profile shape coefficient (–)
λ	Wavelength of incident radiation (μm)

References

1. Zhou, Z., et al. (2023). Vortex generators for passive cooling of rooftop photovoltaic systems under free convection. IEEE Journal of Photovoltaics, 13(5), 743–749.

https://doi.org/10.1109/JPHOTOV.2023.3299752
2. Fathabadi, H. (2021). Novel silica-based PV glass cover providing higher radiative cooling and power production compared with state-of-the-art glass covers. IEEE Journal of Photovoltaics, 11(6), 1485–1492. https://doi.org/10.1109/JPHOTOV.2021.3113160
3. Kim, D. H., Kwak, H., Kim, M. S., & Song, Y. M. (2025). Advanced transparent radiative coolers: Materials, design, and applications. IEEE Journal of Selected Topics in Quantum Electronics, 31(6), 9900114. https://doi.org/10.1109/JSTQE.2025.3585564
4. Zhou, Z., Jiang, Y., Ekins-Daukes, N., Keevers, M., & Green, M. A. (2021). Optical and thermal emission benefits of differently textured glass for photovoltaic modules. IEEE Journal of Photovoltaics, 11(1), 131–137. https://doi.org/10.1109/JPHOTOV.2020.3033390
5. Dosymbetova, G., et al. (2023). Neural network-based active cooling system with IoT monitoring and control for LCPV silicon solar cells. IEEE Access, 11, 52585–52602. https://doi.org/10.1109/ACCESS.2023.3280265
6. de Arrieta, I. G., Echániz, T., Fuente, R., & López, G. A. (2024). Angle-resolved direct emissivity measurements on unencapsulated solar cells for passive thermal control. IEEE Journal of Photovoltaics, 14(3), 459–465. https://doi.org/10.1109/JPHOTOV.2024.3372329
7. Hirst, L. C., Fujii, H., Wang, Y., Sugiyama, M., & Ekins-Daukes, N. J. (2014). Hot carriers in quantum wells for photovoltaic efficiency enhancement. IEEE Journal of Photovoltaics, 4(1), 244–252. https://doi.org/10.1109/JPHOTOV.2013.2289321
8. Legendre, J., & Chapuis, P.-O. (2025). CRESCENT-1D: A 1-D solver of coupled charge and light transport in heterostructures for the design of near-field thermophotonic engines. IEEE Transactions on Electron Devices, 72(3), 1211–1220. https://doi.org/10.1109/TED.2025.3528870
9. Yang, K., Wu, X., Zhou, L., et al. (2025). Towards practical applications of radiative cooling. Nature Reviews Clean Technology, 1, 235–254. https://doi.org/10.1038/s44359-025-00041-5
10. Lee, M., Kim, G., Jung, Y., et al. (2023). Photonic structures in radiative cooling. Light: Science & Applications, 12, 134. https://doi.org/10.1038/s41377-023-01119-0
11. Li, L., Zhang, Q., Liu, G., et al. (2025). Advanced passive daytime radiative cooling: from material selection and structural design to application towards multifunctional integration. Advanced Composites and Hybrid Materials, 8, 97. https://doi.org/10.1007/s42114-024-01127-7
12. Asokan, J., Kumar, P., Arjunan, G., et al. (2025). Photocatalytic performance of spinel ferrites and their carbon-based composites for environmental pollutant degradation. Journal of Cluster Science, 36, 42. https://doi.org/10.1007/s10876-024-02754-2
13. Yu, Z., Wang, B., Gui, L., et al. (2024). Development of photocatalytic and electrocatalytic coatings via thermal spraying for environmental and energy storage applications: a short review. Surface Science and Technology, 2, 7. https://doi.org/10.1007/s44251-023-00030-5
14. Rana, G., Viswanathan, K., Dhiman, V., et al. (2025). Photocatalytic degradation of VOCs: Emerging trends in visible light catalyst modifications and surface engineering. Journal of Cluster Science, 36, 76. https://doi.org/10.1007/s10876-025-02799-x
15. Duda, A., Kopyciński, B., Hawełek, Ł., et al. (2024). Preparation, characterization, and photocatalytic performance of atmospheric plasma-sprayed TiO_2 /Al_2O_3 coatings on glass substrates. Archives of Civil and Mechanical Engineering, 24, 142. https://doi.org/10.1007/s43452-024-00938-1
16. Castañeda de la Hoya, F. M., Torres-Delgado, G., Hernández-García, F. A., et al. (2025). Photocatalytic degradation of 2,4-Dichlorophenoxyacetic acid using ZnO in thin

film: Effect of sintering temperature and irradiation source. Journal of Materials Science: Materials in Electronics, 36, 1292. https://doi.org/10.1007/s10854-025-15363-0

17. Adibekyan, A., Schumacher, J., Pattelli, L., et al. (2025). Emissivity and reflectivity measurements for passive radiative cooling technologies. International Journal of Thermophysics, 46, 66. https://doi.org/10.1007/s10765-025-03532-6
18. Xue, P., Shen, Y., Ye, S., et al. (2023). Secondary solar heat gain modelling of spectral-selective glazing based on dynamic solar radiation spectrum. Building Simulation, 16, 2211–2224. https://doi.org/10.1007/s12273-023-0986-4
19. Grbčić, L., Park, M., Elzouka, M., et al. (2025). Inverse design of photonic surfaces via multi fidelity ensemble framework and femtosecond laser processing. npj Computational Materials, 11, 35. https://doi.org/10.1038/s41524-025-01518-4
20. Li, Y., Wang, F., Zhang, A., et al. (2024). Performance of the multilayer film for infrared stealth based on VO_2 thermochromism. Journal of Thermal Science, 33, 1312–1324. https://doi.org/10.1007/s11630-024-1998-9
21. Liang, J., Tan, X., Dai, Q., et al. (2025). A composite photonic structure with periodic array of SiO_2 particles for solar cell radiative cooling. Applied Physics A, 131, 308. https://doi.org/10.1007/s00339-025-08391-4
22. Yadav, D. K., Malakar, S., Arora, V. K., et al. (2024). Evacuated tube solar collector-based drying system: Analytical modeling, influencing factors, and recent progress in drying of agri-commodities. Food Engineering Reviews, 16, 567–594. https://doi.org/10.1007/s12393-024-09382-6
23. Ramirez-Cuevas, F. V., Gurunatha, K. L., Li, L., et al. (2024). Infrared thermochromic antenna composite for self-adaptive thermoregulation. Nature Communications, 15, 9109. https://doi.org/10.1038/s41467-024-53177-6
24. Grosso, G., Moldaschl, T., Fuger, R., & Binder, A. (2021). Multiphysics reduced order modelling of a packaged laser diode. In 2021 27th International Workshop on Thermal Investigations of ICs and Systems (THERMINIC) (pp. 1–6). IEEE. https://doi.org/10.1109/THERMINIC52472.2021.9626505
25. Zhao, X., Xu, Y., & Hopkins, D. C. (2016). Advanced multi-physics simulation for high performance power electronic packaging design. In 2016 International Symposium on 3D Power Electronics Integration and Manufacturing (3D-PEIM) (pp. 1–5). IEEE. https://doi.org/10.1109/3DPEIM.2016.8048203.
26. Jia, B., Yang, H., Wang, Z., Wang, Y., & Lu, W. (2024). Evolutions of surface charge distribution on DC GIL insulators under electro-thermal coupling field. In 20th International Conference on AC and DC Power Transmission 2024 (pp. 1338–1341). IET. https://doi.org/10.1049/icp.2024.2472
27. Viarengo, S., et al. (2023). A new coupled electrodynamic T–A and thermal model for the critical current characterization of high-temperature superconducting tapes and cables. IEEE Access, 11, 107548–107561. https://doi.org/10.1109/ACCESS.2023.3321194
28. Suresh, K., & Parimalasundar, E. (2022). IPWM Based IBMSC DC-AC Converter Using Solar Power for Wide Voltage Conversion System. *Canadian Journal of Electrical and Computer Engineering*, *45*(4), 394–400. https://doi.org/10.1109/icjece.2022.3207873
29. Zhu, E., Zong, Z., Li, E., et al. (2025). Frequency transfer and inverse design for metasurface under multi-physics coupling by Euler latent dynamic and data-analytical regularizations. Nature Communications, 16, 2251. https://doi.org/10.1038/s41467-025-57516-z
30. Zhang, B., Ma, J., Kou, Y., et al. (2025). Modelling of the electrical-magnetic-thermal-mechanical coupling behavior for the coil-structure electromagnetic launch. Computational Mechanics, 76, 1–22. https://doi.org/10.1007/s00466-024-02584-z
31. Du, W., Sun, L., & Ma, Z. (2025). Multiphysics coupling analysis and structure optimization of flux switching permanent magnet linear motors. Scientific Reports, 15, 21001. https://doi.org/10.1038/s41598-025-04518-y

32. Yujiao, Z., Yinghao, L., Sizhe, N., et al. (2024). Multi-physics coupling simulation of GMAW arc and droplet behaviors based on CFD. Welding in the World, 68, 2589–2610. https://doi.org/10.1007/s40194-024-01806-5
33. Kang, X., Tong, Y., Wu, W., et al. (2023). Transient multi-physics behavior of an insert high temperature superconducting no-insulation coil in hybrid superconducting magnets with inductive coupling. Applied Mathematics and Mechanics - English Edition, 44, 255–272. https://doi.org/10.1007/s10483-023-2960-6
34. Sutanto, B., et al. (2025). Three-dimensional multi-physics modelling and optimisation of a hybrid of radiation filtering and passive cooling strategy for floating photovoltaic systems. Scientific Reports, 15, 27112. https://doi.org/10.1038/s41598-025-10409-sutanto
35. Shao, Q. (2025). Optimization method for geometric shape of DC GIL insulators based on electric thermal multi-physics field coupling model. Electrical Engineering, 107, 3425–3434. https://doi.org/10.1007/s00202-024-02680-6
36. Dan, Q. (2024). Multi-objective optimization of photovoltaic power plant layout planning and system efficiency in waterworks. In 2024 International Conference on Computers, Information Processing and Advanced Education (CIPAE) (pp. 554–559). IEEE. https://doi.org/10.1109/CIPAE64326.2024.00107
37. Wang, X., Duan, Y., Xiao, B., Zhou, Z., Peng, H., & Wang, Y. (2019). Hybrid solar power system optimization based on multi-objective PSO algorithm. In 2019 Chinese Automation Congress (CAC) (pp. 4176–4180). IEEE. https://doi.org/10.1109/CAC48633.2019.8997401
38. Ouhsiane, L., Siroux, M., Ganaoui, M. E., & Mimet, A. (2018). Multi-objective optimization of hybrid PVT solar panels. In 2018 International Conference and Utility Exhibition on Green Energy for Sustainable Development (ICUE) (pp. 1–5). IEEE. https://doi.org/10.23919/ICUE-GESD.2018.8635683
39. Phonrattanasak, P., Miyatake, M., & Sakamoto, O. (2013). Optimal location and sizing of solar farm on Japan east power system using multi-objective Bees algorithm. In 2013 IEEE Energytech (pp. 1–6). IEEE. https://doi.org/10.1109/EnergyTech.2013.6645334
40. Khelifa, A., & Bounib, M. (2023). Intelligential method optimization for improve heat transfer in solar hybrid collector. In 2023 1st International Conference on Renewable Solutions for Ecosystems: Towards a Sustainable Energy Transition (ICRSEtoSET) (pp. 1–4). IEEE. https://doi.org/10.1109/ICRSEtoSET56772.2023.10525485
41. Huang, J., Chen, M., & Xu, D. (2020). An optimization design method of front-stage DC/DC converters for PV system. In 2020 IEEE 9th International Power Electronics and Motion Control Conference (IPEMC2020-ECCE Asia) (pp. 1722–1728). IEEE. https://doi.org/10.1109/IPEMC-ECCEAsia48364.2020.9367944
42. Haridy, S., Radwan, A., Kemel, A., Abo Zahhad, E. M., El-Sharkawy, I. I., & Shamsuzzaman, M. (2025). Enhancing the thermo-electrical performance of low-concentrator photovoltaic module using design of experiments. In 2025 9th International Conference on Green Energy and Applications (ICGEA) (pp. 1–5). IEEE. https://doi.org/10.1109/ICGEA64602.2025.11009242
43. Zhao, S., Li, Q., Sun, Y., et al. (2025). Application of multi-objective optimization based on Sobol sensitivity analysis in solar single-double-effect LiBr-H_2O absorption refrigeration. Frontiers in Energy, 19, 69–87. https://doi.org/10.1007/s11708-024-0938-4
44. Athia, N., Pandey, M., & Saxena, S. (2024). Multi-objective optimization through experimental technical investigation of a green hydrogen production system. Environment, Development and Sustainability. https://doi.org/10.1007/s10668-024-05767-athia
45. Wang, X., & Li, Y. (2025). Design of intelligent energy management system for electric vehicles based on multi-objective optimization. Energy

Informatics, 8, 93. https://doi.org/10.1186/s42162-025-00547-z

46. Aburabi'e, M., Bataineh, K., & Al-Kabaha, Y. (2025). Multi objective design optimization of residential buildings: Energy consumption, life cycle cost and thermal discomfort based on NSGA-II. Innovative Infrastructure Solutions, 10, 354. https://doi.org/10.1007/s41062-025-02158-9
47. Mohan, G. B., Kumar, R. P., & Elakkiya, R. (2025). Enhancing pre-trained models for text summarization: A multi-objective genetic algorithm optimization approach. Multimedia Tools and Applications, 84, 29949–29965. https://doi.org/10.1007/s11042-024-20374-w.
48. Hashemian, N., & Noorpoor, A. (2019). Assessment and multi-criteria optimization of a solar- and biomass-based multi-generation system: Thermodynamic, exergoeconomic and exergoenvironmental aspects. Energy Conversion and Management, 195, 788–797. https://doi.org/10.1016/j.enconman.2019.05.039.